Using a quartz paraboloid for versatile wide-field TIR microscopy with sub-nanometer localization accuracy

René Schneider,[1,2] Tilman Glaser,[3] Michael Berndt,[1] and Stefan Diez[1,2,*]

[1] *Max Planck Institute of Molecular Cell Biology and Genetics, Pfotenhauerstraße 108, 01307 Dresden, Germany*
[2] *B CUBE - Center for Molecular Bioengineering, Technische Universität Dresden, Arnoldstraße 18, 01307 Dresden, Germany*
[3] *Carl Zeiss Jena GmbH, Carl-Zeiss-Promenade 10, 07745 Jena, Germany*
[*] *diez@bcube-dresden.de*

Abstract: Illumination based on objective-type total internal reflection (TIR) is nowadays widely used in high-performance fluorescence microscopy. However, the desirable application of such setups for dark-field imaging of scattering entities is cumbersome due to the spatial overlap of illumination and detection light, which cannot be separated spectrally. Here, we report a novel TIR approach based on a parabolically shaped quartz prism that allows for the detection of single-molecule fluorescence as well as single-particle scattering with high signal-to-noise ratios. We demonstrate homogeneous and spatially invariant illumination profiles in combination with a convenient control over a wide range of illumination angles. Moreover, we quantitatively compare the fluorescence performance of our setup to objective-type TIR and demonstrate sub-nanometer localization accuracies for the scattering of 40 nm gold nanoparticles (AuNPs). When bound to individual kinesin-1 motors, the AuNPs reliably report on the characteristic 8 nm stepping along microtubules.

©2013 Optical Society of America

OCIS codes: (110.0180) Microscopy; (110.2945) Illumination design; (180.2520) Fluorescence microscopy; (260.6970) Total internal reflection; (290.5850) Scattering, particles.

References and links

1. M. Leeuwenhoek and R. de Graaf, “A Specimen of Some Observations Made by a Microscope,” Philos. Trans. Roy. Soc. A. **8**(92-100), 6037–6038 (1673).
2. G. Nomarski, “From phase contrast to contrast by interference,” Rev. Hematol. (Paris) **12**(4), 439–442 (1957).
3. M. Minsky, “Microscopy apparatus,“ U.S. Patent 3,013,467, filed November 7, 1957, and issued December 19, 1961.
4. I. Newton, *Opticks* (William Innys, London, 1704).
5. D. Axelrod, “Cell-substrate contacts illuminated by total internal reflection fluorescence,” J. Cell Biol. **89**(1), 141–145 (1981).
6. D. Axelrod, T. P. Burghardt, and N. L. Thompson, “Total internal reflection fluorescence,” Annu. Rev. Biophys. Bioeng. **13**(1), 247–268 (1984).
7. D. Axelrod, “Total internal reflection fluorescence microscopy in cell biology,” Traffic **2**(11), 764–774 (2001).
8. R. M. Fulbright and D. Axelrod, “Dynamics of nonspecific adsorption of insulin to erythrocyte membranes,” J. Fluoresc. **3**(1), 1–16 (1993).
9. T. Lang, I. Wacker, J. Steyer, C. Kaether, I. Wunderlich, T. Soldati, H. H. Gerdes, and W. Almers, “Ca2+-triggered peptide secretion in single cells imaged with green fluorescent protein and evanescent-wave microscopy,” Neuron **18**(6), 857–863 (1997).
10. U. Resch-Genger, M. Grabolle, S. Cavaliere-Jaricot, R. Nitschke, and T. Nann, “Quantum dots versus organic dyes as fluorescent labels,” Nat. Methods **5**(9), 763–775 (2008).
11. C. Joo, H. Balci, Y. Ishitsuka, C. Buranachai, and T. Ha, “Advances in single-molecule fluorescence methods for molecular biology,” Annu. Rev. Biochem. **77**(1), 51–76 (2008).
12. X. Wang, X. Ren, K. Kahen, M. A. Hahn, M. Rajeswaran, S. Maccagnano-Zacher, J. Silcox, G. E. Cragg, A. L. Efros, and T. D. Krauss, “Non-blinking semiconductor nanocrystals,” Nature **459**(7247), 686–689 (2009).
13. M. A. van Dijk, A. L. Tchebotareva, M. Orrit, M. Lippitz, S. Berciaud, D. Lasne, L. Cognet, and B. Lounis, “Absorption and scattering microscopy of single metal nanoparticles,” Phys. Chem. Chem. Phys. **8**(30), 3486–

#173856 - $15.00 USD Received 14 Jan 2013; revised 14 Jan 2013; accepted 21 Jan 2013; published 5 Feb 2013

3495 (2006).
14. G. Mie, "Beiträge zur Optik trüber Medien, speziell kolloidaler Metallösungen," Ann. Phys-Berlin **330**(3), 377–445 (1908).
15. H. Ueno, S. Nishikawa, R. Iino, K. V. Tabata, S. Sakakihara, T. Yanagida, and H. Noji, "Simple dark-field microscopy with nanometer spatial precision and microsecond temporal resolution," Biophys. J. **98**(9), 2014–2023 (2010).
16. M. van 't Hoff, M. Reuter, D. T. F. Dryden, and M. Oheim, "Screening by imaging: scaling up single-DNA-molecule analysis with a novel parabolic VA-TIRF reflector and noise-reduction techniques," Phys. Chem. Chem. Phys. **11**(35), 7713–7720 (2009).
17. H. Schneckenburger, "Total internal reflection fluorescence microscopy: technical innovations and novel applications," Curr. Opin. Biotechnol. **16**(1), 13–18 (2005).
18. T. Ruckstuhl, M. Rankl, and S. Seeger, "Confocal TIRF microscopy of single molecules," P. Soc. Photo-Opt. Ins., Proc. of SPIEE **4962**, 126–134 (2003).
19. T. Ruckstuhl and S. Seeger, "Confocal total-internal-reflection fluorescence microscopy with a high-aperture parabolic mirror lens," Appl. Opt. **42**(16), 3277–3283 (2003).
20. H. Välimäki and K. Tappura, "A novel platform for highly surface-sensitive fluorescent measurements applying simultaneous total internal reflection excitation and super critical angle detection," Chem. Phys. Lett. **473**(4-6), 358–362 (2009).
21. C. M. Winterflood, T. Ruckstuhl, D. Verdes, and S. Seeger, "Nanometer axial resolution by three-dimensional supercritical angle fluorescence microscopy," Phys. Rev. Lett. **105**(10), 108103 (2010).
22. E. Lassila, T. Alahautala, and R. Hernberg, "Focusing diode lasers using a truncated paraboloid with spherical output surface," Opt. Eng. **46**(5), 054301 (2007).
23. A. L. Mattheyses, K. Shaw, and D. Axelrod, "Effective elimination of laser interference fringing in fluorescence microscopy by spinning azimuthal incidence angle," Microsc. Res. Tech. **69**(8), 642–647 (2006).
24. R. Fiolka, Y. Belyaev, H. Ewers, and A. Stemmer, "Even illumination in total internal reflection fluorescence microscopy using laser light," Microsc. Res. Tech. **71**(1), 45–50 (2008).
25. C. Gell, M. Berndt, J. Enderlein, and S. Diez, "TIRF microscopy evanescent field calibration using tilted fluorescent microtubules," J. Microsc. **234**(1), 38–46 (2009).
26. W. P. Ambrose, P. M. Goodwin, and J. P. Nolan, "Single-molecule detection with total internal reflection excitation: Comparing signal-to-background and total signals in different geometries," Cytometry **36**(3), 224–231 (1999).
27. S. Verbrugge, S. M. J. L. van den Wildenberg, and E. J. G. Peterman, "Novel ways to determine kinesin-1's run length and randomness using fluorescence microscopy," Biophys. J. **97**(8), 2287–2294 (2009).
28. G. I. Mashanov, D. Tacon, M. Peckham, and J. E. Molloy, "The spatial and temporal dynamics of pleckstrin homology domain binding at the plasma membrane measured by imaging single molecules in live mouse myoblasts," J. Biol. Chem. **279**(15), 15274–15280 (2004).
29. T. Ruckstuhl, J. Enderlein, S. Jung, and S. Seeger, "Forbidden Light Detection from Single Molecules," Anal. Chem. **72**(9), 2117–2123 (2000).
30. J. Enderlein and T. Ruckstuhl, "The efficiency of surface-plasmon coupled emission for sensitive fluorescence detection," Opt. Express **13**(22), 8855–8865 (2005).
31. A. Yildiz, M. Tomishige, R. D. Vale, and P. R. Selvin, "Kinesin walks hand-over-hand," Science **303**(5658), 676–678 (2004).
32. A. R. Dunn and J. A. Spudich, "Dynamics of the unbound head during myosin V processive translocation," Nat. Struct. Mol. Biol. **14**(3), 246–248 (2007).
33. R. E. Thompson, D. R. Larson, and W. W. Webb, "Precise nanometer localization analysis for individual fluorescent probes," Biophys. J. **82**(5), 2775–2783 (2002).
34. R. Swaminathan, C. P. Hoang, and A. S. Verkman, "Photobleaching recovery and anisotropy decay of green fluorescent protein GFP-S65T in solution and cells: Cytoplasmic viscosity probed by green fluorescent protein translational and rotational diffusion," Biophys. J. **72**(4), 1900–1907 (1997).
35. F. Ruhnow, D. Zwicker, and S. Diez, "Tracking single particles and elongated filaments with nanometer precision," Biophys. J. **100**(11), 2820–2828 (2011).
36. J. W. J. Kerssemakers, E. L. Munteanu, L. Laan, T. L. Noetzel, M. E. Janson, and M. Dogterom, "Assembly dynamics of microtubules at molecular resolution," Nature **442**(7103), 709–712 (2006).
37. M. J. Schnitzer and S. M. Block, "Kinesin hydrolyses one ATP per 8-nm step," Nature **388**(6640), 386–390 (1997).
38. C. Gell, V. Bormuth, G. J. Brouhard, D. N. Cohen, S. Diez, C. T. Friel, J. Helenius, B. Nitzsche, H. Petzold, J. Ribbe, E. Schäffer, J. H. Stear, A. Trushko, V. Varga, P. O. Widlund, M. Zanic, and J. Howard, "Microtubule dynamics reconstituted in vitro and imaged by single-molecule fluorescence microscopy," Methods Cell Biol. **95**, 221–245 (2010).
39. K. R. Rogers, S. Weiss, I. Crevel, P. J. Brophy, M. Geeves, and R. Cross, "KIF1D is a fast non-processive kinesin that demonstrates novel K-loop-dependent mechanochemistry," EMBO J. **20**(18), 5101–5113 (2001).
40. W. Haiss, N. T. K. Thanh, J. Aveyard, and D. G. Fernig, "Determination of Size and Concentration of Gold Nanoparticles from UV-Vis Spectra," Anal. Chem. **79**(11), 4215–4221 (2007).

#173856 - $15.00 USD Received 14 Jan 2013; revised 14 Jan 2013; accepted 21 Jan 2013; published 5 Feb 2013

1. Introduction

The advent of light microscopy dates back to the late 1600's performed by Leeuwenhoek [1]. In this historical context it seems surprising that about 300 years later decisive progressions have still been made, such as differential-interference contrast microscopy by Georges Nomarski in 1957 [2] or confocal microscopy by Marvin Minsky in 1961 [3]. One of the more recent developments, which turned into textbook knowledge, is the application of evanescent fields (notably described already by Sir Isaac Newton in 1704 [4]) to total internal reflection (TIR) microscopy as presented by Daniel Axelrod in 1981 [5]. In TIR microscopy a laser beam is guided under shallow angles onto an interface separating a substrate from a medium with lower refractive index. Above a critical angle-of-incidence (AOI) the impinging laser beam is totally reflected. However, part of the light penetrates the medium with the lower refractive index in the form of an exponentially decaying evanescent field. This allows illumination of entities, e.g. fluorescent or scattering probes, which are within a layer of approximately 100 nm (the so-called 'penetration depth'). Entities further away from the interface are not illuminated.

In the first TIR microscopes, laser light was guided onto the interface by a variety of prism-shapes made of glass or quartz. The construction of right-angle or trapezoidal prisms was easy and the optics theory well described (see [6] for an excellent review). Among the applications of prism-type TIR microscopes in biology, material science, and medicine [6,7] are studies regarding surface interactions of ligands with lipid membranes [8], cell adhesion to substrates [5], and vesicle transport inside cells [9]. Despite these successful experiments, prism-type TIR microscopy is nowadays only a side arm of the imaging community and no prism-type TIR microscope has made the step into the commercial market.

This stagnation in development originated from recent achievements in constructing high numerical aperture (NA) objectives that enable the setup of objective-type TIR microscopes. In particular, when the NA exceeds the refractive index of the medium to be penetrated, shallow-angle illumination above the critical AOI – and thus TIR illumination – can be achieved by guiding a thin laser beam through the periphery of the objective's pupil. Objective-type TIR has now become the method of choice for fluorescence applications in cell biology for the following reasons: (i) The technique is easily implemented into existing microscopes because the laser beam is brought to the back-focal plane of the objective by simple insertion of an optical element (such as a dichroic mirror) into the illumination path. (ii) Changing the AOI is achieved easily by moving the laser beam within the back-focal plane of the objective. Connected to that is a change in penetration depth that is crucial for quantitative microscopy. Quite importantly, during this procedure the illuminated area remains at the same location, a fact not readily achieved with commonly used right-angle or trapezoidally shaped prisms in prism-type TIR. (iii) Using an inverted microscope, cell experiments in open dishes are possible because both, illumination and imaging, occur from the bottom. Consequently, objective-type TIR operation is facile and requires only low pre-adjustment, driving the penetration of the market with commercial systems for already more than ten years [7].

Nonetheless, illumination and detection paths overlap in objective-type TIR. The particular strengths of this method therefore lies in imaging fluorescent probes, where excitation and emission wavelengths differ from each other, hence rendering spectral separation possible. Unfortunately, commonly used organic dyes, fluorescent proteins or quantum dots suffer from photobleaching, photon blinking, fluorescence saturation, and/or a low number of photons being generated upon excitation [10–12]. These features impose restrictions when fast and precise localization or long-term observation of single molecules or particles is desired. Serendipitously, these disadvantages can be overcome by a multitude of scattering probes, out of which gold nanoparticles (AuNPs) are among the most-promising ones [13]. AuNPs exhibit a large scattering cross section in the visible part of the optical

#173856 - $15.00 USD Received 14 Jan 2013; revised 14 Jan 2013; accepted 21 Jan 2013; published 5 Feb 2013

spectrum due to plasmon resonance [14], provide long-term stability and allow for a versatile surface chemistry. Furthermore, because generation of photons relies on elastic scattering, AuNP emission rates do not saturate. However, scattering probes are hard to incorporate into objective-type TIR setups because the totally reflected beam remains in the detection path and – having the same wavelength – dominates over the scattered signal. If the totally reflected beam were to be reliably blocked only a restricted observation area would remain [15]. Interestingly, this problem is solved in prism-type TIR where the totally reflected illumination beam is naturally rejected from entering the detection path.

Here, in an attempt to revive prism-type TIR microscopy, we present a novel approach based on a parabolically shaped quartz prism that allows for the detection of single-molecule fluorescence as well as single-particle scattering with high signal-to-noise ratios (SNRs). Due to the parabolic shape of the prism, adjusting the AOI (an thus the penetration depth of the evanescent field) is straightforward as it only necessitates the translational movement of the incoming laser beam in one direction (see also [16], where a similar strategy based on a parabolically shaped mirror has been used for the high-throughput imaging of single DNA molecules). During this procedure, the illuminated area remains at the same location, which circumvents the major drawback of right-angle or trapezoidal prisms formerly applied. Moreover, our setup can be adjusted readily and requires only low constructional efforts. In the following, we (i) report on the optical and geometrical properties of our setup, (ii) quantitatively compare the detection efficiencies and SNRs of prism- and objective-TIR microscopy, and (iii) demonstrate localization accuracies down to 0.5 nm for substrate-attached 40 nm AuNPs. When these AuNPs were attached to the tails of individual kinesin-1 motor proteins walking along microtubules (MTs), we readily observed the characteristic 8-nm steps.

2. Design and working principle of parabolic prism-type TIR

Parabolically shaped surfaces are attractive for microscopy applications because they focus light which travels parallel to the optical axis of the paraboloid into the focal spot and, vice versa, light emanating from the focal spot leaves the paraboloid in parallel to the optical axis [6,16–22]. Taking advantage of these properties, we constructed a parabolic quartz prism, where the AOI of the illumination light could be adjusted between 45° and 72° by translational movement of a single mirror (Fig. 1(a)).

2.1 Optomechanical properties of the parabolic prism

The prism, custom-made by precise asphere shaping utilizing high-end grinding and polishing processes at Carl Zeiss Jena GmbH (Jena, Germany) consists of a single piece of quartz with refractive index of $n_{\text{quartz}} = 1.46$ (Fig. 1(b)). The upper part of the prism is cylindrically shaped with a height of 17.3 mm and a diameter of 17.9 mm. The cylindrical shape merges into the parabolically shaped bottom part that has a height of 8.9 mm. The analytical function f(x), which describes the parabolic surface along the x-direction is given by

$$\mathrm{f}(x) = \frac{x^2}{7.2\,\text{mm}} - 2.22\,\text{mm}, \tag{1}$$

where x denotes the distance of the mirror from the optical axis. To allow coupling of the laser beam into a glass-made microscopic flow cell placed underneath the prism, the apex of the prism was cut off creating a polished surface with a diameter of 8 mm. The small size of this contact region enabled the illumination of various fields of interest on an 18 x 18 mm^2 cover slip, forming the topside of the flow cell.

#173856 - $15.00 USD Received 14 Jan 2013; revised 14 Jan 2013; accepted 21 Jan 2013; published 5 Feb 2013

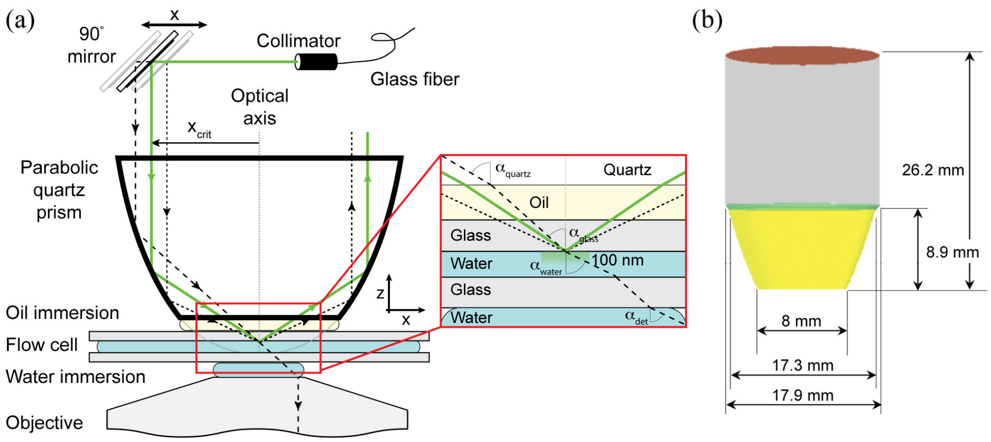

Fig. 1. Design and application of parabolic prism-type TIR. (a) Collimated illumination light is vertically directed into the parabolic quartz prism by a 90° mirror which can be moved horizontally. Depending on the position of the mirror, the beam enters the prism at different distances from the optical axis (dashed black, solid green, and dotted black lines). They are totally reflected at different positions on the parabolic surface and reach the spatially invariant focal spot at the glass-water interface with different angles. Various modes of illumination (e.g. TIR illumination for angles larger than the critical angle) are achievable. Imaging is carried out on an inverted microscope through the objective from the bottom. (b) Constructional sketch of the parabolic quartz prism whose parabolic part (yellow, described by Eq. (1) has a circular bottom surface of 8 mm in diameter and stretches up to a height of 8.9 mm, where a sharp transition (green) leads into a cylindrically shaped part (grey). The laser beam enters and leaves the prism through the top surface (brown).

The range of horizontal distances from the optical axis at which a laser beam can enter the parabolic prism and impinge onto the parabolically shaped curvature is limited from 4.2 mm to 8.2 mm. Using geometrical optics and Eq. (1), a given horizontal distance can be translated into an AOI inside the quartz prism α_{quartz} by Eq. (2) (see inset of Fig. 1(a) for definition of angles):

$$\alpha_{\text{quartz}}(x) = 2 \cdot \left| \arctan\left(-\frac{1}{\mathrm{f}'(x)} \right) \right| \cdot \frac{360^\circ}{2\pi}. \tag{2}$$

Here, $\mathrm{f}'(x)$ denotes the first derivative of Eq. (1). For the horizontal distances given above, this angle reaches from 80° to 47° degree. For TIR to occur at the upper glass-water interface, the laser beam has to pass from the quartz prism into immersion oil and needs to further penetrate into the top glass cover slip of the flow cell. Due to the different refractive indices of the quartz material, the immersion oil (Zeiss Immersol 518F, $n_{\text{oil}} = 1.52$) and the glass cover slip ($n_{\text{glass}} = n_{\text{oil}} = 1.52$), the angles calculated with Eq. (2) are subject to refraction. This was accounted for by applying Snell's law to α_{quartz} using the following equation:

$$\alpha_{\text{glass}} = \arcsin\left(\sin\left(\alpha_{\text{quartz}}\right) \cdot {}^{n_{\text{quartz}}}\!/_{n_{\text{glass}}} \right). \tag{3}$$

Here, α_{glass} denotes the AOI inside the glass cover slip and was calculated to reach from 72° to 45°. Given a critical angle of $\alpha_{\text{crit}} = \arcsin(n_{\text{water}}/n_{\text{glass}}) = 61^\circ$ at the sample interface (here: glass-water with refractive indices of $n_{\text{water}} = 1.33$ and $n_{\text{glass}} = 1.52$) TIR illumination was possible for AOIs above this value. Dependent on the NA of the imaging objective, smaller AOIs resulted in dark- or bright-field illumination. Coupling the parabolic quartz prism to the top of the flow cell at variable heights by immersion oil – with refractive index equal or larger

Received 14 Jan 2013; revised 14 Jan 2013; accepted 21 Jan 2013; published 5 Feb 2013
(C) 2013 OSA

than that of quartz – allowed to always position the focal spot exactly at the glass-water interface.

2.2 Variation of the illuminated area

The size of the illuminated area could be varied by an adjustable fiber collimator to which the single-mode fiber was coupled (see Materials and Methods section). We used 40 nm AuNPs (Fig. 2(a)) and fluorescently labeled streptavidin molecules (Fig. 2(b)) unspecifically attached to the glass surface of the flow cell to measure the illumination areas obtainable with our setup. The minimum size of the illuminated area, approximated by a 2D-Gaussian, was found to be in the order of 90 x 35 μm^2 at the glass-water interface. This illumination area is smaller than the ones typically obtained by conventional objective-type TIR setups and may provide an advantage for applications where large optical power densities in the sample plane are desired. We expect the minimal illumination area to depend on the focusing properties of the collimator in use. The elongated shape of the illuminated area followed from two reasons: First and foremost, the illumination light impinges onto the glass-water interface with a finite AOI. Therefore, a horizontal cross section through the beam profile creates an elliptically shaped area, leading to stronger confinement in y-direction. Second, the curvature of the parabolic surface perpendicular to the optical axis is higher than the curvature parallel to the optical axis. This again leads to enhanced focusing in y-direction. Defocusing the laser beam by means of the adjustable fiber collimator allowed continuous variation of the illumination area up to a size larger than 130 x 130 μm^2. We note that all illumination profiles observed in our experiments exhibited a high degree of homogeneity. Uneven illumination, interference fringes and effects of shadowing, which are often inherent to conventional objective-type TIR setups, due to refractive index inhomogeneities in the illumination pathway [23,24], are thus avoided in our parabolic prism-type TIR setup.

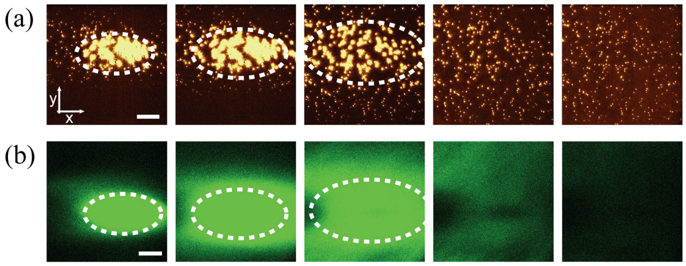

Fig. 2. The size of the illumination area can be varied by the adjustable fiber collimator. Substrate-attached 40 nm AuNPs (a) and fluorescent streptavidin molecules unspecifically adsorbed to the substrate surface (b) were illuminated with a 532 nm laser and 488 nm laser, respectively. The illumination area was increased from a minimal size of 90 x 35 μm^2 up to larger than 130 x 130 μm^2 (left to right). Bar size: 25 µm.

2.3 Variation of the AOI

A unique property that distinguishes our parabolic-prism approach from other, e.g. triangular or trapezoidal prism-type approaches is the fact, that the AOI of the illumination light can be varied by the one-dimensional, translational movement of a single mirror. We tested this by measuring the influence of the AOI on the scattered intensity of surface-immobilized 200 nm Tetraspeck beads (Fig. 3(a)). The AOIs were measured accurately to within 0.5°, by converting the horizontal displacement of the 90° mirror using Eq. (2) and Eq. (3). For AOIs below the critical angle, dark-field illumination was achieved as long as the illumination light was not captured by the imaging objective. The water-immersion objective used in our studies had a NA of 1.2, which corresponds to a maximum opening angle in water of $\alpha_{\text{det}} = 64.4°$ (and using Snell's law an angle in glass of $\alpha_{\text{glass}} = 52°$). The measurement of the scattering intensity of the 200 nm Tetraspeck beads was therefore limited to AOIs above approximately

50° (Fig. 3(b)). Varying the AOI starting from low sub-critical to high super-critical angles lead to a pronounced enhancement in the average scattered intensity and decreased rapidly when the critical angle was exceeded. The data was fitted with the corresponding Fresnel equations for sub- and super-critical angle illumination yielding a critical angle of 63°. This compares well to the theoretical value of the critical angle for a glass-water interface of 61° (see [25] for comparison). The slight deviation from the theoretical value is attributed (i) to uncertainties in the refractive indices of the used glass cover slips and the aqueous medium inside the flow cell and (ii) to imperfect angle measurements. A third contribution to the deviation arose from a slight shift of the illumination spot along the *x*-axis (approximately 10 µm) when the AOI was varied from 45° to 72°. Shifting of the illumination spot was due to imperfections in the actual beam path, mainly caused by the mismatch of the refractive indices between glass, oil and quartz. However, the 10–µm shift of the illumination spot can be avoided when using quartz cover slips (see section 3.2) and did not play a significant role in the actual experiments because the illumination spot was expanded to a much larger area of 130 x 130 μm^2.

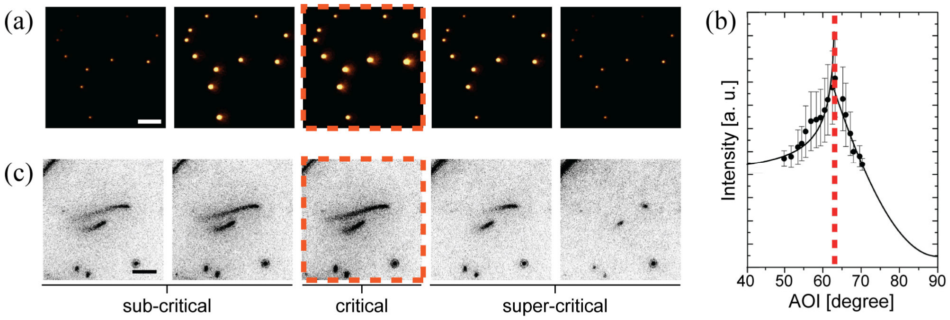

Fig. 3. The AOI can be varied using the translational movement of the 90° mirror. We recorded the scattering of surface-bound 200 nm Tetraspeck beads (a) and the fluorescence of rhodamine-labeled MTs (c), bound to the glass surface with one end and pointing away from the surface with their remaining parts in a tilted orientation, while successively increasing the AOI from low, sub-critical angles (left) to high, super-critical angles (right). Bar size: 25 µm and 10 µm. (b) The scattered intensity (mean ± sd, $N = 262$ beads) showed a clear peak at the critical angle of 63° (red dashed line).

2.4 Variation of the penetration depth

Accompanying a change in the AOI, the penetration depth of the illumination light changed as demonstrated by the use of fluorescently labeled MTs (Fig. 3(c)). MTs primarily landed end-on, causing the remaining parts of the MTs to point away from the surface in a tilted orientation. Similar to previous results, where tilted MTs had been used to measure and calibrate the TIR penetration depths [25], a clear change in MT appearance became visible when successively increasing the AOI from low, sub-critical angles to high, super-critical angles. For sub-critical angles ($\alpha_{\text{glass}} < \alpha_{\text{crit}}$), the parts of the MTs near the surface appeared with moderate intensities. The imaging contrast smoothly decreased along the lengths of the tilted MTs due to defocussing and background excitation. At the critical angle ($\alpha_{\text{glass}} = \alpha_{\text{crit}}$), the fluorescence intensity near the surface reached a maximum. The penetration depth became finite leading to vertically restricted excitation of the tilted MTs as well as the background. For super-critical angles ($\alpha_{\text{glass}} > \alpha_{\text{crit}}$), the fluorescence intensity near the surface remained high but decayed rapidly along the MTs due to the decreased penetration depth.

3. Quantitative comparison of detection efficiencies in TIRF microscopy

Due to the different geometries of the illumination pathways in prism- and objective-type TIR (Fig. 4(a) and 4(b)), both approaches differ in the detection efficiency of single-molecule fluorescence. However, to our knowledge, comparative studies of prism- and objective-type

TIR fluorescence (TIRF) microscopy, in particular considering the illumination and detection geometries, are rarely being found [26]. To benchmark our parabolic-prism setup to the objective-type TIR setup, we investigated the SNRs in images obtained from individual eGFP-labeled kinesin-1 molecules attached to surface-immobilized MTs.

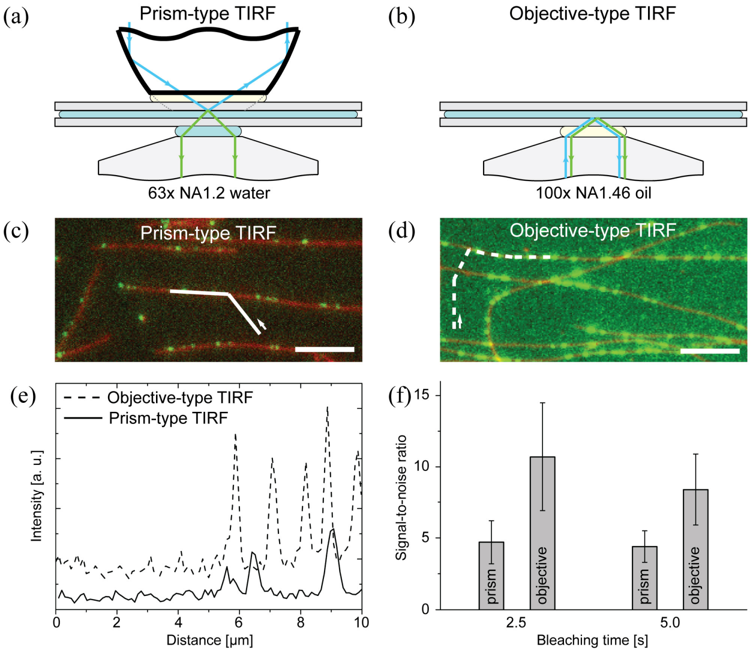

Fig. 4. Comparison of prism- and objective-type TIRF. Illustration of the parabolic prism-type (a) and objective-type TIRF (b) setups where critical-angle illumination (blue line) is performed on the far side (a) and the near side (b) of the objective, respectively. Single-molecule fluorescence (green line) is captured using a 63x NA1.2 water objective (a) and a 100x NA1.46 oil objective (b). Example images of individual eGFP-labeled kinesin-1 motor molecules (green) immobilized on MTs (red) in the presence of the non-hydrolyzable ATP-analogue AMP-PNP using parabolic prism-type (c) and objective-type TIRF (d). The illumination laser powers were adjusted such that equal bleaching times occurred in both setups. Bar size: 5 µm. (e) Intensity line scans taken from (c) and (d) showing lower background levels and lower noise for prism-type TIRF (solid curve) but higher signal amplitudes for objective-type TIRF (dashed curve). (f) Comparison of SNRs calculated from experiments performed at bleaching times of 2.5 s and 5.0 s shows lower SNRs for prism-type TIRF as compared to objective-type TIRF.

To allow for a fair comparison, it is not sufficient to adjust equal laser powers entering the quartz prism or the microscope objective; instead the power density of the evanescent fields need to be equalized. We therefore developed a method based on the bleaching times of the investigated fluorescent molecules: because the bleaching times deterministically decrease with increasing power density [27,28], we argue that equal bleaching times correspond to equal power densities in the evanescent fields. For both setups, we maximized the eGFP signal by adjusting the AOI to the critical angle and avoided premature bleaching. For the results to be evaluated in the following we adjusted the laser powers such that the eGFP molecules bleached within 2.5 ± 0.3 s (mean ± sd; N = 225 molecules) and 2.5 ± 0.1 s (N = 362) for prism-type and objective type TIRF, respectively (see Fig. 4(c)-4(e) for typical images and intensity line scans obtained under these conditions and the Materials and Methods section). It appeared that prism-type TIRF performed superior in terms of (i) low background levels, defined by the mean pixel intensity values in regions without fluorescent molecules (about one third compared to objective-type TIRF) and (ii) low noise levels, defined by the standard deviation of pixel intensity values in regions without fluorescent molecules (about one half compared to objective-type TIRF). On the other hand, objective-type TIRF produced higher intensity amplitudes (i.e. higher peak intensities), obtained by fitting Gaussians to the pixel intensity values of fluorescent molecules (about four times compared to prism-type TIRF). Based on this nomenclature, we defined the SNR of a molecule as: (intensity amplitude – background) / noise. Using prism-type TIRF, we obtained an SNR of 4.8 ± 1.5 (mean ± sd), in contrast to objective-type TIRF with an SNR of 10.7 ± 3.8 (Fig. 4(f)). At bleaching times of 5 s, the SNRs decreased to 4.4 ± 1.1 ($N = 61$, prism-type TIRF) and 8.4 ± 2.5 ($N = 375$, objective-type TIRF). At equal power densities, objective-type TIRF thus allowed for SNRs approximately 2.1 times larger than prism-type TIRF.

3.1 Noise and SNR depend on square root of amplitude

For the prism- and objective-type TIRF setups investigated in our study, the dependence of the optical noise on the amplitude of the fluorescence intensities was described by the same square-root relationship (Fig. 5).

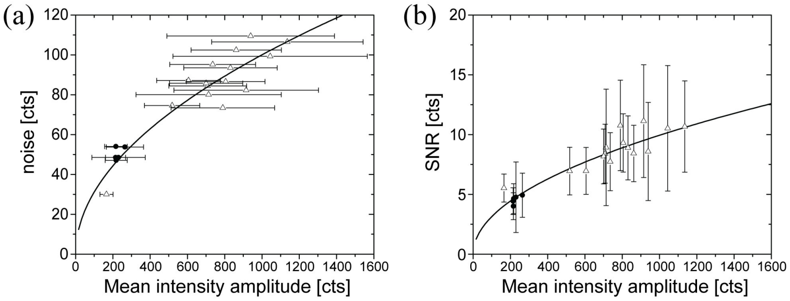

Fig. 5. Noise and SNR depend on the square root of the number of collected photons. (a) The measured noise is plotted versus the mean amplitude of the molecules (mean ± sd; dots - prism-type TIRF, triangles – objective-type TIRF). The data was fit to a square root relationship because a scaling factor of 0.5 was found when fitting the data to a weighted power function. (b) The SNR (mean ± sd) was calculated from the single data points and compared to the calculated SNRs using the square root dependency found in (a). Each data point averages over at least 70 (100) molecules for prism-type (objective-type) TIRF.

Proof for the square-root relationship was found by plotting the noise level b present in the recorded streams versus the mean intensity amplitude of the imaged molecules (Fig. 5(a)). Fitting the data to a power function $\mathrm{f}(x) = y_0 + Bx^C$, yielded the offset value y_0 being equal to zero within the error bars, the exponent C being 0.51 ± 0.04, providing evidence for a square-root dependency, and the factor B being determined to 3.0 ± 0.8. Therefore, the data was well described by the following formula:

$$\text{Noise} = 3\sqrt{\text{Amplitude}}. \tag{4}$$

We calculated the SNR based on the measured noise level and intensity amplitudes of the molecules. We compared the measured SNRs to the calculated SNRs (using Eq. (4) making use of the following equation:

$$\text{SNR} = \frac{\text{Amplitude}}{\text{Noise}} = \frac{\text{Amplitude}}{3\sqrt{\text{Amplitude}}} = \frac{1}{3}\sqrt{\text{Amplitude}}, \tag{5}$$

which is plotted in Fig. 5(b) and, as a consequence, the SNR also depended on the intensity amplitude by the same square-root relationship: on average, four times more photons collected in our objective-type TIRF measurements compared to the prism-type setup thus resulted in an about two times better SNR. We note, that background and noise in the prism-type TIRF setup can be lowered (and thus the SNR increased) when the glass cover slips near

#173856 - $15.00 USD Received 14 Jan 2013; revised 14 Jan 2013; accepted 21 Jan 2013; published 5 Feb 2013
(C) 2013 OSA

the parabolic prism are replaced by quartz cover slips. This way, non-negligible background and noise contributions originating from the intrinsic autofluorescence of glass cover slips would be avoided while keeping the intensity amplitude unchanged. However, quartz cover slips are rather costly, which is why they were not considered in our study aiming at devising a widely applicable imaging system. In order to explain the increased number of detected photons in the objective-type TIRF setup compared to the prism-type TIRF setup, a multitude of factors needs to be considered.

a) Dipole emission pattern near interfaces

(i) The emission patterns of dipoles close (< 50 nm) to an optical interface (e.g. glass-water) is strongly shifted toward the medium with the higher refractive index [29,30]. This leads to enhanced emission toward the glass cover slip and thus the objective in objective-type TIRF. In contrast to that, prism-type collection schemes only harvest the minor part of the emission pattern being emitted toward the optically thinner medium (here: the water medium). We theoretically estimated the percentage of photons being emitted toward the glass cover slip and toward the water to 72% and 28%, respectively [29,30] (i.e. a ratio of about 3 in favor of objective-type TIRF, see Fig. 6).

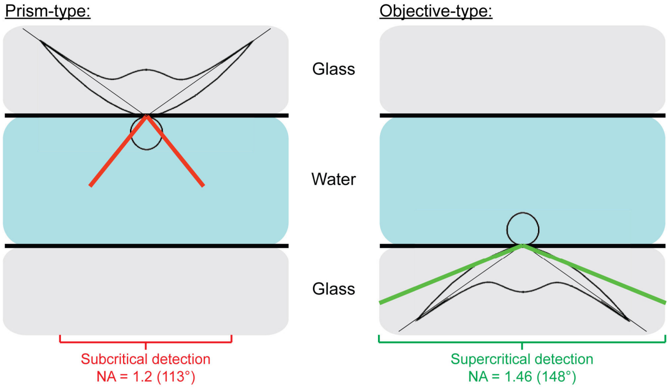

Fig. 6. The emission pattern of a dipole close to an optical interface is distorted toward the optically thicker medium (here: the glass). The distortion leads to increased emission toward the glass medium. This effect favors objective- over prism-type collection schemes in terms of detection efficiency. Dipole emission patterns adapted from [29].

b) NA of the imaging objective

The NAs of the *C-Apochromat 63x/1.2 W Korr* (Zeiss) objective used for prism-type TIRF and the *alpha Plan-Apochromat 100x/1.46* (Zeiss) objective used for objective-type TIRF were different. Consequently, both objectives collect different amounts of light, the ratio of which can be obtained by relating the integral areas of spherical cones with opening angles 2arcsin(NA/n) to each other. In our case, this estimation led to a factor of about 1.3 times more photons being collected in objective-type TIRF.

c) Transmission of objectives and the water layer

In the spectral range of the eGFP emission, the transmission of the high-NA objective used in the objective-type TIRF setup was 0.9 times the transmission of the objective used in the prism-type TIRF setup (data provided by the objective vendors). (iv) Light attenuation through the additional 100 µm layer of water present in the prism-type TIRF setup allowed for a 1.1 times more efficient light capture in the objective-type TIRF setup.

Taken together, we conclude that objective-type TIRF, mainly due to efficient nearfield coupling of molecules to the glass substrate, collects a factor of approximately 3.9-fold (3 × 1.3 × 0.9 × 1.1) more photons than prism-type TIRF. As a consequence, the expected difference in the SNRs for both setups yields a factor of about 2.0 (square root of 3.9), in good agreement with the 2.1-fold difference being experimentally measured. We note that this difference in the SNRs was imposed by our experimental conditions adjusted for equal excitation power densities (as concluded from equal single-molecule bleaching times) in both TIRF setups. When comparing the SNRs under the condition of a 4-fold lower laser power density in the objective-type TIRF setup (i.e. with comparable mean intensity amplitudes in both setups) we indeed measured similar SNRs for objective- and prism type TIRF (Fig. 5).

3.2 Design considerations on using glass vs. quartz cover slips

In the previous sections we aimed at devising a widely applicable prism-type TIRF imaging system. We therefore coupled the parabolic quartz prism to glass cover slips (via immersion oil with $n_{\text{oil}} = n_{\text{glass}} = 1.52$). However, because the autofluorescence of glass is non-negligible, the SNR can be increased by coupling the parabolic quartz prism to quartz cover slips (via an index-matching immersion fluid with $n_{\text{fluid}} = n_{\text{quartz}} = 1.46$). Further advantages of full index-matching ($n = 1.46$) are a yet superior spatial stability of the illumination spot (i.e. it resides at exactly the same position when changing the AOI) as well as an enlarged range of accessible illumination-spot sizes (going along with an enlarged range of excitation power densities at a given laser output power) (see simulations in Fig. 7).

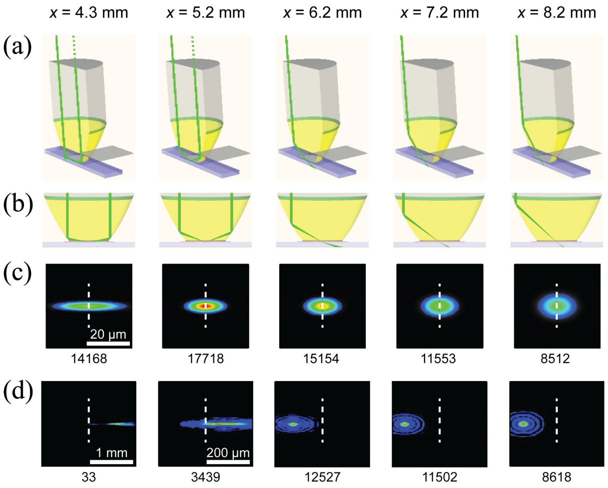

Fig. 7. Simulation of the illumination characteristics for various imaging conditions ($n = 1.46$). (a) Calculated path of a Gaussian laser beam ($1/e^2$ diameter of 0.5 mm) entering the parabolic quartz prism at increasing distances x from the optical axis and hence decreasing AOIs. (b) Zoomed-in side view on the quartz-prism/quartz-cover slip/water interface showing the transition from super- to sub-critical angle illumination (left to right). (c) The profile of the optical power density in the field of view (maximum power density given below in arbitrary units) for the associated configurations in (a) and (b). Note, that the illumination spot stays centered in the field of view (40 x 40 μm^2, dashed line). (d) In contrast, the illumination spot of a collimated beam shifts spatially along the x-axis, when immersion oil ($n_{\text{oil}} = 1.52$) and glass cover slips ($n_{\text{glass}} = 1.52$) are used. Compared to the simulations, a smaller shift by approximately only 10 µm was observed in the experiments. This shift was found to be negligible because for the experiments described in the main text the illumination laser beam was expanded yielding a large illumination area (larger than 130 x 130 μm^2). Simulated results were obtained using FRED (Photon Engineering, Tucson, AZ, USA).

4. Application of parabolic prism-type TIR for sub-nanometer localization of AuNPs

Single-molecule experiments often involve the localization of the imaged entities with a precision well below the pixel size in the image [31,32]. As the localization precision increases with the number of the collected photons [33], AuNPs are promising optical probes because they exhibit an extraordinarily high scattering cross section in the visible part of the

Received 14 Jan 2013; revised 14 Jan 2013; accepted 21 Jan 2013; published 5 Feb 2013
(C) 2013 OSA

optical spectrum. For example, a 40 nm AuNP provides around 300 nm^2 of scattering cross section [13] compared to an absorption cross section of 0.01 nm^2 for an eGFP molecule [34]. Consequently, at equal power densities at least 30,000 times more photons are generated by a 40 nm AuNP compared to an eGFP molecule. To demonstrate this advantage in combination with parabolic prism-type TIR we compared the localization precision of individual eGFP molecules and 40 nm AuNPs in a configuration where both labels were attached to kinesin-1 motor proteins bound to surface-immobilized MTs (Fig. 8(a), see Materials and Methods section).

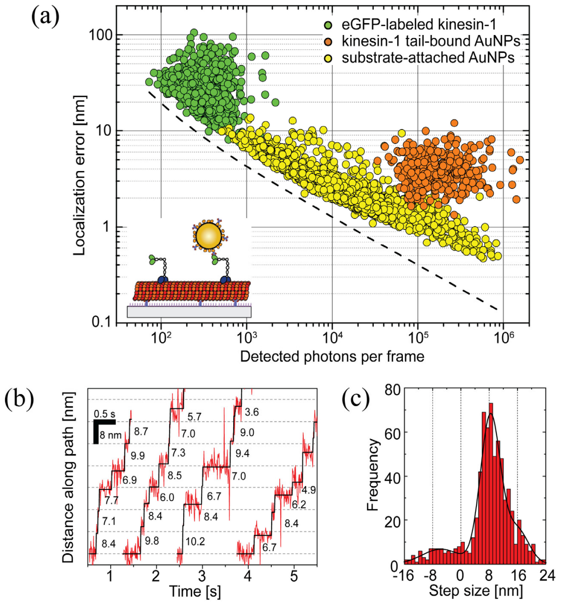

Fig. 8. Localization precision for eGFP molecules and 40 nm AuNPs. (a) Localization errors as functions of the number of detected photons per frame for: eGFP molecules at the tails of kinesin-1 motor proteins bound to substrate-attached MTs (green dots) and 40 nm AuNPs bound to the eGFP molecules (orange dots, see inset for molecular geometries) as well as 40 nm AuNPs directly attached to the substrate (yellow dots). Each dot represents the localization error of an individual eGFP molecule or 40 nm AuNP. Motor proteins were rendered immobile to the MTs by the presence of AMP-PNP. (b) Stepwise motion of 40 nm AuNPs attached to kinesin-1 motors walking along MTs in the presence of 1 µM MgATP (velocity of 17 ± 6 nm/s, mean ± sd, $N = 22$). The distance along the path (red line) was examined with a step-finding algorithm (black line). (c) Histogram of step sizes calculated from 22 AuNPs performing a total of 715 steps. A minor fraction of steps was found at + 16 nm, which corresponds to two consecutive steps that were too fast to be resolved individually.

Moreover, we explored the limits of localization precision by localizing 40 nm AuNPs directly immobilized on the substrate surface. To quantify the localization precision, we determined the center positions of the eGFP molecules and the 40 nm AuNPs by fitting their images to two-dimensional Gaussians using FIESTA tracking software [35] (see Materials and Methods section). The positions obtained in every frame of the acquired image sequence resemble a normal distribution around the mean position with a width that we term the 'localization error'.

Single eGFP molecules attached to kinesin-1 motor proteins on surface-immobilized MTs were localized to a precision of 28 ± 13 nm (mean ± sd, $N_{\mathrm{mol}} = 1009$) by collecting between 100 to 1000 photons within 100 ms of exposure (Fig. 8(a), green dots). Only in the very best cases the localization error was below 10 nm. When streptavidin-conjugated 40 nm AuNPs were loaded onto the tails of kinesin-1 motors via biotinylated anti-eGFP antibodies the localization error was determined to be 3.8 ± 1.8 nm (mean ± sd, $N = 385$, Fig. 8(a), orange

#173856 - $15.00 USD Received 14 Jan 2013; revised 14 Jan 2013; accepted 21 Jan 2013; published 5 Feb 2013

dots). In this case, the number of collected photons ranged from 100,000 to 1,000,000 within 30 ms of exposure (at laser excitation powers approximately 1/10th of the ones used for the localization of the eGFP molecules). For similar numbers of detected photons, substrate-bound 40 nm AuNPs were localized with errors below 1 nm (Fig. 8(a), yellow dots). We attribute this improvement in localization precision to the avoidance of positional fluctuations of the 40 nm AuNPs due to the molecular flexibility of the kinesin-1 tails. In the very best cases, substrate-attached 40 nm AuNPs were localized with a precision of about 5 Å. The dependency of the localization error on the number of collected photons was well predicted by theory [33] over four orders of magnitude (Fig. 8(a), dashed line). The slight deviations of the experimental data from the predicted behavior are assumed to mainly originate from systematic errors in determining the actual photon number (below 10,000 detected photons per frame) and spatial drift (above 10,000 detected photons per frame, see also the Materials and Methods section).

Using 40 nm AuNPs we finally studied the stepping of kinesin-1 motor proteins along MTs. Therefore, the trajectories of 22 transported AuNPs (measured with 15 ms exposure times) were projected onto their linearized path (Fig. 8(b)). A step-finding algorithm [36] was applied and yielded a step size histogram with a major peak at 8.3 ± 4.0 nm (mean ± sd, N = 498 steps, Fig. 8(c), see also the Materials and Methods section), corresponding to the spacing of α-/β-tubulin dimers in a MT protofilament as well as the step sizes formerly obtained using polystyrene beads and quantum dots attached to kinesin-1 tails [31,37]. The broad width of the peak is mainly attributed to the AuNPs being flexibly coupled to the kinesin-1 motors via streptavidin, biotinylated eGFP antibodies, eGFP at the motor tails and the tails themselves (estimated total linker length about 30 nm). Because no external forces are applied, the particles are free to undergo tethered diffusion around the MT-interacting kinesin-1 motor domains. We note that the width of the peak (4.0 nm) is in agreement with the localization accuracy of 3.8 nm obtained for 40 nm AuNPs attached to immobilized kinesin-1 motors. The reduction of localization accuracy due to linkage flexibility can be overcome in setups with external force application, e.g. in optical tweezers. There, the linkage can be strained limiting the tethered diffusion to the direction perpendicular to the applied force. However, this strategy comes at the cost of not being able to measure on a load-free system. A second reason for the broad peak are freely diffusing AuNPs present in the flow channel. These particles occasionally penetrate the observational TIR field and contribute a fluctuating optical background to the image, reducing the ability to precisely localize the AuNPs of interest in each frame. In fact, the latter problem is also present in single-molecule fluorescence experiments, where the localization accuracy likewise decreases in the presence of free fluorophores in solution.

5. Summary

We developed a quartz-based, parabolic prism-type, wide-field TIR setup enabling the detection of single-molecule fluorescence and single-particle scattering with high SNRs. Due to the parabolic shape of the prism, adjusting the penetration depth of the evanescent field, while keeping the illuminated area at the same location, can be achieved by the translational movement of only one mirror. Construction of the device, easily implementable into any commercial microscope in place of the usual bright-field condenser, is straightforward. In comparison to objective-type TIR setups, our approach (i) allows to work at AOIs well exceeding the critical angle for TIR, thus making the illumination of ultra-thin sample layers possible and (ii) enables the detection of scattering signals with low background.

To quantitatively compare the performance of prism-type and objective-type TIR setups in fluorescence applications we introduced a novel calibration method based on the characteristic bleaching times of single molecules. We found that objective-type TIRF generally collects more photons than prism-type TIRF, mainly because near-field-emission into the glass substrate (i.e. into the direction of the image-collecting objective) is enhanced

#173856 - $15.00 USD Received 14 Jan 2013; revised 14 Jan 2013; accepted 21 Jan 2013; published 5 Feb 2013

[30]. On the other hand, prism-type TIR setups exhibit lower background signals due to the decoupling of illumination and detection light paths. The decoupling of illumination and detection light paths also becomes of interest for the imaging of scattering probes where no spectral separation between illumination and emission light is possible. Prism-type TIR is thus the method of choice for the imaging of scattering probes, which naturally overcome the intrinsic limitations of photobleaching, photon blinking, and saturation inherent to fluorescent probes.

Using the scattered light of 40 nm AuNPs illuminated by the parabolic prism-type TIR setup with exposure times in the range of 10 ms we achieved localization accuracies below 1 nm. This high accuracy relies on the facts (i) that the peak positions of Gaussian photon distributions can be localized with much smaller errors than the optical resolution limit and (ii) that the localization error scales inversely with the square root of the number of collected photons. The large scattering cross section of AuNPs gives them a distinct advantage with regard to the latter criterion. Proving the applicability of these particles for the detection of conformational changes of biomolecules, we successfully imaged the characteristic 8-nm steps of individual kinesin-1 motor proteins walking along the surface of MTs. For the future, we foresee an enormous potential for scattering nanoparticles to replace organic dyes, fluorescent proteins, and quantum dots in single-molecule experiments. The development of high-performance and easy-to-use imaging devices, such as the parabolic prism-type TIR setup described here, are expected to accelerate this development.

6. Materials and methods

6.1 Optomechanical setup

All optical components were mounted in a micro bench system (LINOS, Göttingen, Germany) where the cylindrical part of the prism was fixed to a custom-made base plate. The position of the quartz prism along the optical axis was adjusted using a fine micrometer screw. A single-mode FC/PC glass fiber (OZ Optics, Ottawa, Canada, article no.: LPSC-04-400/700-3.5/125-P-6AC-11-40-3S-3AS-10 with an NA of 0.1) was coupled to the system via an adjustable fiber collimator (LINOS, Focusing Collimator MB 02 FC0/PC0, Order No. G169003000), which allowed for focusing of the laser beam. Mounting to the upper arm of an inverted Axiovert 200M microscope (Zeiss, Göttingen, Germany) was achieved using a custom-made adapter.

6.2 Microscopic flow-cell experiments

All experiments were performed in flow cells constructed from 22 x 22 mm^2 and 18 x 18 mm^2 glass cover slips (#1.5, Gerhard Menzel Glasbearbeitungswerk GmbH & Co. KG, Braunschweig, Germany) and 1 mm wide stripes of double-sided sticky tape (tesa, Hamburg, Germany). Glass cover slips were rendered hydrophobic before use by treatment with dichlorodimethyl-silane (DDS, Sigma). Typically, the channels were 18 mm in length, 2 mm in width and 100 µm in height resulting in an inner volume of approximately 4 µL [38]. The standard buffer solution in our experiments was BRB80 (80 mM potassium PIPES, pH 6.9, 1 mM EGTA, 1 mM $MgCl_2$).

6.3 Fluorescent and scattering probes

Two different probes were used as *surface-immobilized scatterers*: 40 nm streptavidin-coated AuNPs (British Biocell International, Cardiff, UK) as well as 100 nm and 200 nm Tetraspeck beads (Invitrogen, Carlsbad, CA, USA). For immobilization of the 40 nm streptavidin-coated AuNPs and the Tetraspeck beads the stock solutions were diluted 1000-fold in BRB80, flushed into a channel of a flow cell and incubated for 30 seconds and 5 minutes, respectively. Unbound AuNPs (beads) were removed by washing with 20 µL BRB80. Channels were readily sealed using nail polish on either side of the channel to prevent evaporation.

#173856 - $15.00 USD Received 14 Jan 2013; revised 14 Jan 2013; accepted 21 Jan 2013; published 5 Feb 2013

Fluorescent microtubules were polymerized from 5 μL of a 1:3 mixture of rhodamine-labeled and unlabeled porcine brain tubulin (4 mg/mL, self-made tubulin purification) in BRB80 with 4 mM $MgCl_2$, 1 mM MgGTP, and 5% DMSO. After 30 minutes, microtubule polymers were stabilized by the addition of BRB80T (BRB80 with 10 μM taxol) and stored at room temperature. Microtubules were always made freshly before each experiment. For the SNR measurements and the stepping assays we expressed a truncated, e*GFP-labeled rat kinesin-1* construct (rkin430eGFP) [39], which is dimeric and contains the first 430 amino acids of conventional kinesin-1 fused to an eGFP domain and a polyhistidine tag at the tail. *Antibody-conjugated AuNPs* where prepared from 40 nm streptavidin-conjugated AuNPs and biotinylated eGFP antibodies (from MPI-CBG, batch number 106A20). A volume of 500 μL of the streptavidin-conjugated AuNP stock solution was centrifuged for 3 minutes at 10.000g, and, after collecting the supernatant, resuspended to the same volume of BRB80T with 1% Tween20. Repeating this procedure three times ensured reduction of free streptavidin and sodium azide to a minimum. We then mixed 10 μM of biotinylated anti-eGFP antibody with the AuNP solution in a ratio of 180 antibodies per AuNP, and kept it in a fridge over night. The next morning, AuNPs were again centrifuged three times for 3 minutes at 10.000g to reduce the amount of yet unbound antibodies. In a last centrifugation step we reduced the total volume to 50 μL and measured the concentration of AuNPs in a spectrometer according to the method described in [40]. The final concentration of antibody-conjugated AuNPs was typically in the 10 nM range. When loading AuNPs to motor proteins, various ratios, ranging from 1:1 to 10:1, of antibody-conjugated AuNPs to kinesin-1 were incubated for 15 minutes on ice and always the lowest ratio that still produced transported AuNPs was used.

6.4 Kinesin-motor stepping assays

For rkin430eGFP stepping assays the flow cell was washed with a sequence of buffers to allow fluorescent microtubules to bind to the glass substrate. First, a solution of β-tubulin antibodies (0.5% SAP.4G5, Thermo Fisher Scientific) diluted in BRB80 was incubated for 5 minutes, followed by a washing step with BRB80. The channel was then incubated with 1% Pluronic F127 in BRB80 for 15 minutes. Subsequently, the channel was washed with 80 μL of BRB80T. A solution of microtubules was flushed in and was allowed to adsorb for 1 minute. Unbound microtubules were removed from the channel by washing with 40 μL BRB80T. The microtubule density on the glass substrate was checked under the microscope before continuing with the flow sequence. To allow AuNP-loaded motor proteins to bind to the microtubule lattice we flushed in 20 μL of 300 pM AuNP-loaded rkin430eGFP in imaging buffer (265 μg/mL Casein, 47 mM Glucose, 130 μg/mL Glucose Oxidase, 24 μg/mL Catalase, 12 mM DTT, 1.2% Tween20, and 1.2 μM MgATP in BRB80T).

6.5 Imaging

Image acquisition was performed using an inverted Axiovert 200M microscope (Zeiss, Göttingen, Germany) in combination with an Andor iXon DV 897 electron multiplied (EM) CCD camera (Andor, Belfast, Northern Ireland). Image capture was performed using the imaging software MetaMorph (Molecular Devices, Sunnyvale, CA, USA). The microscope was equipped with a Lumen 200 metal arc lamp (Prior Scientific Instruments, Jena, Germany) to provide fluorescence in epi-illumination.

Fluorescence imaging with prism-type TIR microscope: For excitation of eGFP-labeled proteins (FITC-labeled streptavidin) we used the 488 nm laser line of a fiber-coupled Innova 70C spectrum laser (Coherent, Santa Clara, CA, USA). The following filters were used for imaging: Ex 488/10, Dic 505LP, Em 515/30, all from Chroma (Bellows Falls, VT, USA). The EM gain of the CCD camera was varied between 100x and 300x. For excitation of 100 nm Tetraspeck beads and rhodamine-labeled microtubules we used the 530 nm laser line of the Innova 70C spectrum laser. The following filters were used for imaging: Ex 535/50, Dic

#173856 - $15.00 USD Received 14 Jan 2013; revised 14 Jan 2013; accepted 21 Jan 2013; published 5 Feb 2013

565LP, Em 610/75, all from Chroma. Fluorescence was collected using a 63x C-Apochromat 1.2W Korr (Zeiss, Göttingen, Germany).

Fluorescence imaging with objective-type TIR: For objective-type TIRF we used a slider system (Zeiss, Göttingen, Germany), which was connected to the fiber-coupled Innova 70C spectrum laser. Focusing of illumination light and detection of fluorescence was achieved using a 100x alpha Plan-Apochromat NA1.46 (Zeiss, Göttingen, Germany). The power of the illumination light was measured with a power meter when the laser beam exited the TIRF objective in a straight line.

Scattering imaging with prism-type TIR microscope: For illumination of AuNPs (100 nm and 200 nm Tetraspeck beads) we used the 530 nm laser line of the Innova 70C spectrum laser. Scattered light was collected using a 63x C-Apochromat 1.2W Korr. No additional spectral filters were used and the EM gain of the camera was set to 1x. For stepping assays with AuNP-loaded motors, half of the 512 x 512 pixel camera chip was utilized to achieve exposure times of down to 15 ms. The brightness of the AuNPs was adjusted by varying the power of the 530 nm laser, which was measured with a power meter just before the laser beam entered the parabolic prism.

6.6 Bleaching assays

The bleaching times of immobile eGFP-labeled motor proteins were measured in a stepping assay configuration. We incubated microtubule-decorated channels for 1 minute with 300 pM rkin430eGFP in the presence of 10 μM AMP-PNP, a slowly hydrolyzable ATP analogue, followed by washing with 20 μL imaging buffer. Upon laser illumination with 488 nm, single-molecule bleaching events were imaged by continuous streaming with 100 ms exposure times. We measured the decay in fluorescence intensity along the microtubules over time and fitted a mono-exponential function to yield the characteristic decay constant τ_{bleach}. We proved for the individuality of the molecules by detecting several two-step bleaching processes characteristic for the dimeric rkin430eGFP molecules. To match the imaging pixel size of the camera to 102 nm (100 nm) per pixel we placed an additional 2.5x (1.6x) lens in the detection path of the 63x water objective (100x oil-objective) used for prism-type (objective-type) TIRF. All measurements where performed within the same time span right after flushing in the final imaging solution (typically 5-10 minutes). The camera settings for both setups were exactly the same. The parabolic prism-type TIR setup was compared to objective-type TIR setups at excitation powers that caused equal bleaching times.

The background level and the associated noise were determined by calculating the mean and the standard deviation of the pixel intensity values in regions without fluorescent molecules. The bleaching of 225 (362) molecules was imaged using the parabolic prism-type (objective-type) TIR setup and quantified using FIESTA tracking software [35]. Fitting Gaussians to the pixel intensity values of single molecules yielded intensity amplitudes (height of Gaussian above the background) of 240 ± 78 (1136 ± 406) counts, background levels of 177 (497) counts with a noise b of 50 (107) counts. The measured widths of the Gaussians differed only slightly for both setups (prism-type: 135 ± 19 nm, N = 225, objective-type: 131 ± 13 nm, N = 362, mean ± sd), however we found that the width was not important for the determination of the difference in SNRs between both setups. Therefore, the intensity amplitude rather than the volume intensity was used as a measure for the number of photons being collected.

6.7 Localization of point-like objects

To study the localization accuracy of the AuNPs (eGFP-labeled motor proteins) we collected movie streams with exposure times of 10 to 100 ms (100 ms) and excitation powers between 100 μW to 2 mW (1 mW to 5 mW). *Image analysis* was performed using FIESTA tracking software, which fits two-dimensional Gaussians to the pixel intensity values of the object and extracts the center position (x_i- and y_i-coordinate) of the intensity maximum, the width σ_i of

#173856 - $15.00 USD Received 14 Jan 2013; revised 14 Jan 2013; accepted 21 Jan 2013; published 5 Feb 2013

the distribution, and the intensity amplitude A_i of the maximum above background in every i-th frame. The distribution of the center positions in every frame resembles a symmetrical two-dimensional Gaussian around the mean position whose width, which we call 'localization error', was estimated by using a Maximum-Likelihood method. The pixel size of the camera, the sensitivity of the chip, and the applied magnification was used to convert the volume under the fitted distribution into the number of detected photons per frame. We corrected for stage drift by separately tracking the positions of 100 nm Tetraspeck beads. The dependency of the experimentally determined localization errors on the number of detected photons was compared to a theoretical expression [33]:

$$\langle \Delta x \rangle = \sqrt{\frac{\sigma^2 + a^2/12}{N} + \frac{8\pi\sigma^4 b^2}{a^2 N^2}}. \tag{6}$$

Here, σ describes the width of the fitted Gaussian, a the pixel size of the camera, N the number of detected photons, and b the background noise. The parameters used in Eq. (6) were determined to $\sigma = 122.9$ nm, $a = 101.6$ nm, and $b = 2$ photons and resulted in good agreement with the experimental data (Fig. 8(a), dashed line). The effect of the background noise b on the localization error $<\Delta x>$ becomes negligible when the number of detected photons N is large ($b^2/N^2 \to 0$). Therefore, the background noise was estimated from the eGFP molecules rather than the bright AuNPs. Selecting those molecules and particles that (i) showed less than 3000 photons per frame and (ii) were localized best in a certain interval of photon counts enabled analysis of the factor by which Eq. (6) missed the data. This factor was determined to 1.5 ± 0.1 (mean ± sd, N = 54 localized objects). The localization error of AuNPs attached to the tail of immobile kinesin-1 via biotinylated anti-eGFP antibodies was measured with 30 ms exposure time and a histogram of the localization errors showed a log normal distribution (data not shown).

For step detection, 22 AuNPs, which were transported along microtubules with a velocity of 17 ± 6 nm/s (mean ± sd) at 1.2 μM MgATP, were tracked. We averaged the complete path of each molecule to a line and projected the movement of the AuNP onto that path. We then used a step-finding algorithm [36] to find step-like motion in the 'distance along the path' data. This step-finding algorithm does not make an assumption about the step size. Evaluation of the step sizes of the 22 tracks was performed carefully by (i) displaying the 'distance along the path' data versus time, without scale bars as to not provide a bias for 8 nm distances and (ii) the step size histogram was displayed only at the end of the whole evaluation (no in-between checking for 8 nm peaks). By successively increasing the sampling rate of the algorithm we were able to reject traces, which showed oversampling. Regardless of the sampling rate we found that a majority of 8 nm steps was found in all traces. The step size distribution was fit to a three-peak Gaussian and yielded peaks at −5.5 nm, 8.3 nm and 16.5 nm.

Acknowledgments

The authors wish to thank Dr. Volkmar Giggel (Carl Zeiss Jena GmbH, Jena) for the fabrication of the quartz paraboloid, as well as Tiemo Anhut (Carl Zeiss MicroImaging GmbH, Jena) and Brüne Venus (Carl Zeiss MicroImaging GmbH, Göttingen) for fruitful discussions. This work was financially supported by the ERC (starting grant 242933), the DFG (Heisenberg program, Research Unit 877 and grant DI 1226/3), the Technische Universität Dresden and the Max-Planck-Society.